Author(s): Miettunen, Kati & Halme, Janne & Visuri, Anne-Maria & Lund, Peter

Title: Two-Dimensional Time-Dependent Numerical Modeling of Edge Effects in Dye Solar Cells

Year: 2011

Version: Post print

Please cite the original version:

Miettunen, Kati & Halme, Janne & Visuri, Anne-Maria & Lund, Peter. 2011. Two-Dimensional Time-Dependent Numerical Modeling of Edge Effects in Dye Solar Cells. Journal of Physical Chemistry C. Volume 115, Issue 14. 7019-7031. ISSN 1932-7447 (printed). DOI: 10.1021/jp110927j.

Two-dimensional time-dependent numerical modeling of edge effects in dye solar cells

Kati Miettunen,* Janne Halme, Anne-Maria Visuri, Peter Lund

New Energy Technologies Group, Department of Applied Physics, Aalto University, P.O.Box 15100 FI-00076 AALTO, Finland

* corresponding author, email: kati.miettunen@tkk.fi

Abstract

A two-dimensional transient model of dye solar cells (DSC) describing the electrochemical reactions in the cell has been prepared. The model includes the relevant components of DSCs: the photoelectrode, the electrolyte, and the counter electrode. The solved variables are potential and the concentrations of the different ion species, which can be used to determine e.g. the current-voltage characteristics of the cell. The largest benefit of this model is its 2D features which enable the study of lateral inhomogeneity. Using the model, a new phenomenon was described: lateral current density distribution caused by a small difference in the size between photoelectrode and counter electrode, typical to laboratory test cells, causes tri-iodide to move from the edge region to the active area of the cell. This process takes relatively long time (8 min) and can be important for performance characterization and design of DSCs.

Notation

Symbols

A	active area	m^2
a	absorption coefficient	$1/m$
C	capacitance	F
c	concentration	mol/m^3
D	diffusion coefficient	m^2/s
d	distance between the electrode substrates	m
d_{CE}	thickness of the counter electrode	m
d_{PE}	thickness of the photoelectrode	m
E_F	Fermi energy	eV
F	Faraday constant	C/mol
f	$F/(R_{gas}T)$	1/V
i	current density	A/m^3
i_{lim}	limiting current density	A/m^2
i_0	exchange current density	A/m^3
K	equilibrium constant	
k	reaction rate constant	1/s
k_B	Boltzmann constant	J/K
m	ideality factor	
$\mathbf{N}$	ion flux	$mol/(m^2s)$
n	number of transferred electrons	
Q_j	current source	A/m^3
q	elementary charge	C
R	resistance	Ω
R_{gas}	gas constant	J/(Kmol)
s	stoichiometric coefficient	
T	temperature	K
u_m	mobility	$m^2mol/(Js)$
u	x-velocity	m/s
V	voltage	V
v	y-velocity	m/s
x	distance from the PE substrate	m
z	charge number	
α	transfer coefficient	
δ_{ts}	time-scaling coefficient	
η	overpotential	V
η	efficiency	
η_{OC}	open-circuit voltage	V
λ	wavelength	nm
σ	conductivity	S/m
υ	reaction rate	$mol/(m^3s)$
Φ	incident spectral photon flux	$photons/(m^2s)$
ϕ	electric potential	V
σ_0	Conductivity of TiO_2 at equilibrium	S/m

Subscripts

a	activation
b	backward reaction
CE	counter electrode
CT	charge transfer
col	collection
d	diffusion
el	electrolyte
f	forward reaction
g	generation
i	ion species
inj	injection
LH	light harvesting
IPCE	indicent photon to collected electron
rec	recombination
s	series
0	initial, equilibrium
PE	photoelectrode
ph	photo
t	transport

Abbreviations

ALD	atomic layer deposition
CE	counter electrode
CV	cyclic voltammetry
e^-	electron
DSC	dye solar cell
I	iodine
I^-	iodide
I_3^-	tri-iodide
I-V	current-voltage
O	oxidized species
OC	open circuit
PE	photoelectrode
Pt	platinum
R	reduced species
SC	short circuit
TiO_2	titanium dioxide

1 Introduction

Photoelectrochemical cells such as dye solar cells (DSCs) may become a technically and economically possible alternative to the present-day silicon solar cells. The low-cost fabrication of DSCs due to their simple construction and low-cost materials is a clear advantage. In addition, solar light-to-current conversion efficiencies of over 10 % [1] are adequate for a wider use of the cells. Currently the up-scaling of the DSC technology is a topical issue. In addition to current collection, there are several other challenges such as spatial performance distribution when going for larger scale [2]. In larger area cells, it is important to understand and evaluate the significance of different kinds of inhomogeneity and edge effects. In the investigation of such questions modeling is an efficient tool as it would very difficult or even impossible to obtain the information through measurements. The previously made models have, however, mainly been one-dimensional (1D) and cannot answer such questions. This gives the motivation to develop two-dimensional (2D) models of DSC. In this work we focus on electrochemical 2D modeling which in addition to electrical performance (I-V performance) gives information also on the mass transport in the electrolyte.

The earliest electrochemical models date to the 1990's [3, 4, 5], and some of the very early models are in some part outdated as the knowledge about the reaction mechanisms in DSCs has grown. A good basic one dimensional model was introduced by Ferber *et al.* [4] and it has been used largely as a basis for this work. In that model, the space between the photoelectrode substrate and the counter electrode is filled by a pseudohomogenous medium consisting of porous TiO_2, dye, and electrolyte.

Oda *et al.* continued the basic model by Ferber *et al.* [4] by adding a separate bulk electrolyte layer. Such a layer is also present in the models made by Papageorgiou *et al.*[3] and by Hyk and Augustynski [6]. An additional modification made by Ferber and Luther [7] is the implementation of the Helmholtz layers using the Stern's modification of the Gouy-Chapman theory. The Helmholtz layers describe the double layer charging between two phases. The layers are typically only a few nanometers thick [8] and they can be omitted when studying only microscale ionic distribution of the cells.

In the basic model of Ferber *et al.* [4] and in the extension [7] the only back reaction at the photoelectrode taken into account is the charge recombination from the TiO_2 to the electrolyte. This is usually adequate with the exception that at low light intensities current leakage from the substrate to the electrolyte is typically significant [9, 10, 11] and therefore needs also to be taken into account. There are also a series of other back reactions, such as recombination via oxidized dye, which importance needs to be evaluated on the basis of the employed materials, but with common dyes such as N719 can be assumed negligible.

Dye solar cell models are typically one dimensional. An exception to this the further work by Ferber and Luther [7] in which they separated the TiO_2 and electrolyte to

study the charge transfer processes in those media. That model is in principle two-dimensional, but only describes a very thin ($\sim$ 50 nm) slice of a dye solar cell making it practically only one dimensional. Only quite recently Gagliardi *et al.* [12] published a steady-state 2D in which the TiO_2 and electrolyte still separated but the photoelectrode composed of several columns instead of a single one making the model truly 2D.

Cao *et al.* [13] added the time dependence into the continuity equation describing the charge carrier transport in the TiO_2 film. The model of Cao *et al.* focuses on the photoelectrode and does not describe a complete solar cell. The mathematical formulation presented in their work reduces in steady state to the equations used in the basic model by Ferber *et al.* [4].

Recently, a simple analytical 1D dye solar cell model to simulate I-V curves based on physical parameters was presented [14]. Its relations to electrochemical impedance spectroscopy (EIS) was shown in that work [14].

Here we introduce a two dimensional transient dye solar cell model. The equations in 2D format are solved numerically using the COMSOL Multiphysics modeling software. The spatial distribution of potential and concentrations of the different ion species modeled in a vertical cross-section of the cell. Similar to the previous 1D model [14], the parameters of this model can be largely determined by EIS. To make the application of this model easy, the theory behind the model, the determination of model parameters and the construction of the model using COMSOL Multiphysics are explained in detail. The model is applied to investigate the edge effects in typical cell setup, where the counter electrode is somewhat larger than the photoelectrode. It is shown that the cell geometry has significant effects on the ion concentrations at the active region and the time to reach steady state conditions.

2 Theoretical section

In this model, all the three main components are modelled: the photoelectrode (PE), the counter electrode (CE), and the electrolyte. The photoelectrode is modeled here as a pseudo-homogeneous medium of TiO_2, dye, and redox electrolyte. This composition describes the electrode well and a similar one has been used for the photoelectrode in 1D modeling [4, 15]. The realization of a pseudo-homogeneous electrode with COMSOL is similar to the one used by Hottinen *et al.* in the case of a polymer electrolyte membrane fuel cell model [16].

The dye molecules absorb the incoming photons which is here modeled with the Lambert-Beer law. The excited electrons are injected into the conduction band of the semiconductor. The electrons diffuse through the nanoparticles and are collected at the back contact. The electrons may also leak from the photoelectrode to the electrolyte. The most significant current leakage pathways are from the TiO_2 layer and from the substrate to the I_3^- ions in the electrolyte. There are also a series of other back reactions, such as recombination via oxidized dye, the importance of which needs to be evaluated on the basis of the employed materials, but which for common dyes such as N719 can be assumed negligible. The contact between the TiO_2 and the substrate is assumed ideal. This is in most cases a valid presumption since a TiO_2 - substrate contact resistance has been detected only in the case of few alternative substrates [11, 17].

The electrolyte I^- and I_3^- ions function as mediators for the electrons between the photoelectrode and the counter electrode, i.e. the anode and the cathode. The oxidized dye molecules are reduced with the I^- ions, which, when oxidized, form I_3^- ions. I_3^- is again reduced at the cathode into I^- by the electrons from the external circuit. The total reaction is

$$I_3^- + 2e^- \rightleftharpoons 3I^-, \tag{1}$$

where the net forward reaction occurs at the counter electrode and the net backward reaction at the photoelectrode. The mass transport of the ions is here described by the Nernst-Planck equation and electroneutrality.

At the counter electrode, the substrate is covered with a material of high electrocatalytic activity, usually a Pt layer [18] of a few nanometers or a few micrometers thick porous carbon [19, 20]. The counter electrode can be modeled as an interface (*cf.* Pt) or a as pseoudohomogeous mixture of catalyst and electrolyte (*cf.* porous carbon). The charge transfer at the counter electrode is described by current-overvoltage equation.

The 2D model presented here is to some extent a numerical extension of our previous analytical 1D DSC device model [14], but with the following differences:

Instead of pure diffusion according to the Fick's law assumed in [14], mixed diffusion

and migration according to the using the Nernst-Plack equations are used to model the ionic transport in the electrolyte.

In [14] the effects of electrode porosity on the mass transport in the electrolyte were neglected. Here, they are taken into account similar to Ferber et al. [4], by modeling the electrode domains as overlapping pseudo-homogenous effective media of the electrode and the electrolyte phases. As a result, the local ion concentrations in the pores of the film are calculated as a part of the model solution.

In [14] the effect of electrolyte concentrations on the photoelectrode function was omitted. In the present model, the ion concentrations in the pores of the film are coupled to the interfacial charge transfer reaction (recombination) at the TiO_2 surface through the local over-potential, similar to Ferber et al. [4]. The effect of ion concentration on the charge transfer reaction inside a pore counter electrode are taken into account in a similar fashion.

In [14] the non-ideality of the photoelectrode I-V characteristics was accounted for by adding a posteriori the ideality factor in the mathematical expression for the solar cell I-V curve – an approximation necessary to reach an analytical solution. Here, the non-ideality is introduced as non-linear electron recombination, as proposed by Bisquert and Mora-Seró [21], thus rooting it to a microscopic physical model [22].

Finally, in contrast to [14], the implementation of the model with COMSOL Multiphysics brings about the possibility to run 2D and transient simulations at the macroscopic scale of the solar cell. This is the main new functionality of our model compared to previous numerical DSC models [4], and will be our focus in the practical examples later in the paper.

2.1 Charge and mass transport in the electrolyte

The movement of dissolved ion species in the electrolyte is described by the Nernst-Planck equation

$$\mathbf{N}_i = -z_i u_i F c_i \nabla\phi - D_i \nabla c_i + c_i \mathbf{u}, \tag{2}$$

where $\mathbf{N}_i$ is the ion flux, z_i the charge number, u_i the mobility, c_i the concentration, ϕ the electric potential and D_i the diffusion coefficient of ion species i. The mobilities and diffusion coefficients are related as $D_i = R_{gas} T u_i$ [23], where R_{gas} is the gas constant. F is the Faraday constant and $\mathbf{u}$ the bulk velocity of the solution.

The first term in eq. (2) stands for migration and the second term for diffusion. The third term indicates the motion of the solution with a bulk velocity, i.e. convection. This term is assumed very small and is left out on the grounds of the porosity of the electrodes and the small distance between them [3].

Eq. (2) is valid for dilute solutions, which have been determined as solutions with

solute concentrations below 0.1 M [24, 25, 26]. In this model the concentrations of some ion species are slightly higher, exceeding 0.5 M. However, we anticipate that applying eq. (2) should not cause a significant error. Eq. (2) has been used frequently in electrolyte modeling in similar cases [4, 7, 27, 28].

As chemical reactions are assumed to occur at the electrodes only, no ions are produced nor consumed in the bulk electrolyte,

$$\frac{\partial c_i}{\partial t} + \nabla \cdot \mathbf{N}_i = 0. \tag{3}$$

Eq. (1) states that at the anode, I^- is consumed and I_3^- produced and at the cathode, vice versa. Cations, here Li^+, do not take part in the reactions. The production of ion flux is proportional to the current density per unit volume i due to charge transfer at the electrode-electrolyte interfaces

$$\frac{\partial c_i}{\partial t} + \nabla \cdot \mathbf{N}_i = \frac{s_i}{nF} i, \tag{4}$$

where s_i is the stoichiometric coefficient of species i in the redox reaction (1), $s_{I^-} = -3$, $s_{I_3^-} = 1$ and $s_{Li^+} = 0$.

The bulk electrolyte is assumed to be electrically neutral,

$$\sum_{i=I^-,I_3^-,Li^+} z_i c_i = 0, \tag{5}$$

While electroneutrality is not a fundamental law of nature, it has been observed to apply in all solutions except in a thin electric double layer of 1 to 10 nm near the boundary surfaces of the solution.

2.2 Limiting current density

At sufficiently high currents, the rate of the reaction at the electrodes is no longer controlled by rate of electron transfer but by the rate of the transport of ions to the electrode surfaces. The maximum current density that diffusion can convey is called the limiting current density i_{lim}. Since the c_{I^-} in the electrolyte is typically much larger, here nine times larger, than $c_{I_3^-}$, the current in the cell is limited by the transport of I_3^-. i_{lim} for I_3^- is obtained as [29]

$$i_{lim} = \frac{4FD_{I_3^-}c_{I_3^-,0}}{d}, \tag{6}$$

where F is Faraday's constant, $D_{I_3^-}$ the diffusion coefficient of I_3^-, $c_{I_3^-,0}$ the equilibrium concentration of I_3^- and d the thickness of the electrolyte layer (i.e. distance between the electrode substrates). i_{lim} can be determined from I-V measurements of symmetric CE-CE cells, and when i_{lim} and $c_{I_3^-,0}$ are known, $D_{I_3^-}$ can be calculated using eq. (6) [29].

2.3 Charge-transfer at the counter electrode

The current density per unit volume i_{CE} produced at the counter electrode in a one-electron transfer reaction

$$\mathrm{O} + \mathrm{e}^- \rightleftharpoons \mathrm{R} \tag{7}$$

between an oxidized species O and a reduced species R is described by the current-overpotential equation [8]

$$i_{CE} = i_0 \left[\frac{c_r}{c_{r,0}} e^{-\alpha f \eta_{CE}} - \frac{c_o}{c_{o,0}} e^{(1-\alpha) f \eta_{CE}} \right], \tag{8}$$

where the coefficient i_0 is the exchange current density, $f{=}F/(R_{gas}T)$, c_o and c_r are the concentrations of oxidized and reduced species and $c_{o,0}$ and $c_{r,0}$ their equilibrium (initial) concentrations. α is the transfer coefficient, $\alpha \in [0, 1]$, which determines the symmetry of the overpotential-current curve and η_{CE} is the voltage between the electrolyte and the counter electrode, $\eta_{CE} = \phi_{el} - \phi_{CE}$.

In DSCs, the reaction at the electrodes is not, however, a one-electron reaction but consists of three consecutive steps [30]:

$$(\mathrm{I}^- \rightleftharpoons \mathrm{I} + \mathrm{e}^-) \times 2 \qquad \text{charge-transfer reaction,} \tag{9}$$

$$2\mathrm{I} \rightleftharpoons \mathrm{I}_2 \qquad \text{fast chemical reaction,} \tag{10}$$

$$\mathrm{I}_2 + \mathrm{I}^- \rightleftharpoons \mathrm{I}_3^- \qquad \text{fast chemical reaction.} \tag{11}$$

The reduced and oxidized species of eq. (8) are therefore I^- and I, respectively. The reactions listed above resulting in a half order process are widely used but also first and second order processes have also been suggested [31, 32, 33]. More investigation is apparently still needed to define the correct reactions at each electrode. For the examples shown later in this work, the selection of reaction process should not significantly influence.

Equations (10) and (11) are as fast chemical reactions assumed to be always in equilibrium [4]. Hence, the law of mass action, which describes solutions in dynamic equilibrium, can be applied to the reaction

$$\mathrm{I} \rightleftharpoons \frac{1}{2}\,\mathrm{I}_3^- - \frac{1}{2}\,\mathrm{I}^- \tag{12}$$

and the concentration of I written in terms of the concentrations of I^- and I_3^- and an equilibrium constant K,

$$c_I = K c_{I_3^-}^{\frac{1}{2}} c_{I^-}^{-\frac{1}{2}}. \tag{13}$$

Substituting c_I from eq. (13) and c_{I^-} into eq. (8) gives

$$i_{CE} = i_0 \left[\frac{c_{I^-}}{c_{I^-,0}} e^{-\alpha f \eta_{CE}} - \sqrt{\frac{c_{I_3^-} c_{I^-,0}}{c_{I^-} c_{I_3^-,0}}} e^{(1-\alpha) f \eta_{CE}} \right]. \tag{14}$$

2.4 Charge-transfer resistance at the counter electrode

The value of i_0 needed for eq. (14) can be determined with the charge transfer resistance at counter electrode-electrolyte interface R_{CT}. This can be done by deriving R_{CT} from eq. (14). With small currents, the concentrations of ion species can be approximated with their equilibrium values, which leads to

$$i_{CE} = i_0 \left[e^{-\alpha f \eta_{CE}} - e^{(1-\alpha) f \eta_{CE}} \right] \tag{15}$$

known as the Butler–Volmer equation. The approximation is good when current is less than 10 % of i_{lim} [8].

η_{CE} is a sum of activation overpotential η_a, also called the surface overpotential [23], and concentration overpotential, or diffusion overpotential, η_d. η_a is due to the rate of the charge-transfer reaction at the interface. Whereas when the transfer of ions is not as fast as the charge-transfer reaction would require, the current through the interface becomes limited by diffusion. Here approximating the concentrations with equilibrium ones excludes the mass-transfer effects, and the voltage between the electrode and the electrolyte is then assumed to be the pure activation overpotential, $\eta_{CE} \approx \eta_a$.

The charge-transfer resistance R_{CT} in the case of porous counter electrode can be presented as a resistance corresponding to a unit volume r_{CT}, $r_{CT} = R_{CT} A d_{CE}$, where A is the area and d_{CE} the thickness of the counter electrode. For an interface type counter electrode $r_{CT} = R_{CT} A$. r_{CT}, which thus has the units [Ωm^3] or [Ωm^2] depending on the electrode type, is defined as

$$r_{CT} = -\frac{d\eta_a}{di_{CE}}. \tag{16}$$

Differentiating both sides of eq. (15), we get

$$r_{CT} = -\frac{1}{i_0} \left[-\alpha f e^{-\alpha f \eta_a} - (1-\alpha) f e^{(1-\alpha) f \eta_a} \right]^{-1} \tag{17}$$

and when $\eta_a = 0$,

$$i_0 = \frac{1}{f r_{CT,0}}. \tag{18}$$

Hence i_0 can be determined through measuring the R_{CT} of a symmetric CE-CE cell with impedance spectroscopy in open circuit conditions where $\eta_a = 0$. At open circuit, the both electrodes are assumed to have the same R_{CT} and the resistance of one electrode is half of the measured resistance. i_0 can then be calculated from eq. (18). R_{CT} can also be determined by measuring complete DSCs at open circuit: when there is no current through the cell, the voltage loss takes place at the photoelectrode-electrolyte interface and the overpotential at the counter electrode is zero, as assumed in eq. (18).

2.5 Current generation at the photoelectrode

The current density per unit area generated in the PE at a specific wavelength λ can be written as

$$\int_0^{d_{PE}} i_g(\lambda, x)dx = q\Phi(\lambda)\eta_{LH}(\lambda)\eta_{inj}(\lambda), \tag{19}$$

where i_g is the current density per unit volume, x the distance from the PE substrate, q elementary charge, Φ the incident spectral photon flux, η_{LH} the light-harvesting efficiency, and η_{inj} the electron injection efficiency. η_{LH} is the probability of an incident photon to be absorbed by a dye molecule, which depends on the absorption coefficient of the dye and the thickness of the photoelectrode. η_{inj} is the probability of an excited dye molecule to inject the electron to the TiO_2.

Note that, the incident-photon-to-collected-electron efficiency η_{IPCE} is a product of three terms,

$$\eta_{IPCE}(\lambda) = \eta_{LH}(\lambda)\eta_{inj}(\lambda)\eta_{col}(\lambda), \tag{20}$$

where η_{col} is the collection efficiency. Here η_{col} is in this model taken into account via the analysis of the recombination and transport characteristics of the PE.

The position dependence of η_{LH} can be described with the Beer-Lambert law. The law assumes the absorbing medium to be non-scattering, homogeneous and isotropic. The photoelectrode can usually be approximated to be such with reasonable accuracy. For instance due to the small size of the 20-nm-diameter TiO_2 particles, scattering in the photoelectrode film is negligible [34]. Using the Beer-Lambert law, η_{LH} is

$$\eta_{LH}(\lambda) = \int_0^{d_{PE}} a(\lambda)e^{-a(\lambda)x}dx, \tag{21}$$

where a is the absorption coefficient of the dye. Hence, $i_g(\lambda, x)$ can be written as

$$i_g(\lambda, x) = q\Phi(\lambda)\eta_{inj}(\lambda)ae^{-ax}. \tag{22}$$

Eq. 22 can be used for modeling the current generated by monochromatic light. In the case of a full solar spectrum, the current per unit volume at distance x from the substrate is

$$i_g(x) = q\int_{\lambda_{min}}^{\lambda_{max}} \Phi(\lambda)\eta_{inj}(\lambda)a(\lambda)e^{-a(\lambda)x}d\lambda, \tag{23}$$

where λ_{min} and λ_{max} reflect the spectral response of the dye. Note that the eqs. (23) and (22) take into account only the light that penetrates the photoelectrode for the first time. Secondary effects such as back reflection are not included. The focus of this model is in the mass and change transport and hence detailed optical analysis is omitted here.

2.6 Charge recombination at the photoelectrode

The density of electrons in the conduction band n_e can be written

$$n_e = n_{e,0} e^{\frac{E_F - E_{F,redox}}{k_B T}}. \tag{24}$$

where $n_{e,0}$ is equilibrium density of electrons in the conduction band, E_F Fermi energy, $E_{F,redox}$ the redox Fermi level of the electrolyte, and k_B Boltzmann constant. In terms of energy levels, photovoltage V_{PE} corresponds to the difference of the PE Fermi level and the redox Fermi level of the electrolyte,

$$qV_{PE} = E_F - E_{F,redox}. \tag{25}$$

The concentration and density of electrons in the semiconductor are proportional, and can be written based on eqs. 24 and 25 as

$$c_e = c_{e,0} e^{\frac{qV_{PE}}{k_B T}}. \tag{26}$$

As explained in section 2.3, the charge-transfer from TiO_2 to the electrolyte is an elementary (one-step) reaction described by the chemical equation

$$\mathrm{I}^- \underset{k_b}{\overset{k_f}{\rightleftharpoons}} \mathrm{I} + \mathrm{e}^- \tag{27}$$

where k_f and k_b are the corresponding rate constants. The net reaction rate of the backward direction, i.e. the recombination rate of electrons from the semiconductor to the electrolyte, is

$$v_{net} = k_b c_I {c_e}^{\beta} - k_f c_{I^-}. \tag{28}$$

where we have with factor β taken into account that recombination reaction may not be linear in the electron concentration [21, 22]. At equilibrium, the forward and backward reaction rates are equal,

$$k_b c_{I,0} {c_{e,0}}^{\beta} = k_f c_{I^-,0}. \tag{29}$$

Here $c_{i,0}$ are the equilibrium concentrations. By substituting k_f from eq. (29) into eq. (28) we get

$$v_{net} = k_b \left({c_e}^{\beta} c_I - \frac{{c_{e,0}}^{\beta} c_{I,0}}{c_{I^-,0}} c_{I^-} \right). \tag{30}$$

By inserting c_I from eq. (13) and using eq. (26) for the electron concentration, v_{net} turns into

$$v_{net} = k_b K c_{e,0} \left(\sqrt{\frac{c_{I_3^-}}{c_{I^-}}} e^{\frac{q\beta V_{PE}}{k_B T}} - \sqrt{\frac{c_{I_3^-,0}}{c_{I^-,0}}} c_{I^-} \right). \tag{31}$$

If the net reaction rate is chosen to have a unit [$m^{-3}s^{-1}$], the recombination current i_{rec} per unit volume is v_{net} multiplied by the elementary charge:

$$i_{rec} = i_{rec,0} \left(\sqrt{\frac{c_{I_3^-}}{c_{I^-}}} e^{\frac{q\beta V_{PE}}{k_B T}} - \sqrt{\frac{c_{I_3^-,0}}{{c_{I^-,0}}^3}} c_{I^-} \right), \tag{32}$$

where $i_{rec,0} = q k_b K {c_{e,0}}^{\beta}$.

Considering the recent discussion on the non-linear nature of the electron recombination in DSC [21, 22], it is worth noting that the present numerical model allows replacing eq. (28) in principle with any kind of expression arising from a detailed physical description of the recombination mechanism. For example, Bisquert *et al.* [35] have shown that the exponent β in eq. (28) can be explained with a physical model that assumes that electron recombination occurs mainly via electron trap states distributed exponentially in energy in the band gap of the TiO_2. Note that if variations in the electrolyte concentration can be neglected, i.e. the concentrations are fixed to their equilibrium values, eq. 28 reduces to

$$v_{net} = k_b' \left(c_e^{\beta} - c_{e,0}^{\beta} \right) \tag{33}$$

where $k_b' = k_b c_{I,0}$. From eq. 33, it follows that the recombination current per unit volume becomes

$$i_{rec} = i_{rec,0}' \left(e^{\frac{q\beta V_{PE}}{k_B T}} - 1 \right) \tag{34}$$

where $i_{rec,0}' = q k_b c_{I,0} c_{e,0}^{\beta}$. Eq. (34) is identical to the well know I-V characteristics of a non-ideal diode, where the factor β is often replaced with the ideality factor $m = \beta^{-1}$. While eq. (34) can be used to approximate analytical modeling of DSC, we use here eq. (32) instead, since the concentration variations are solved explicitly as a part of the numerical model.

2.7 Recombination resistance at the photoelectrode

In the eq. 32, there are two unknown parameters, $i_{rec,0}$ and β, that need to be determined experimentally for the model simulations. They can be determined through measuring the recombination resistance R_{rec} of the photoelectrode with impedance spectroscopy. The recombination resistance is a voltage-dependent resistance which limits the recombination current from the photoelectrode to the electrolyte. Here, only the recombination from TiO_2 to the electrolyte is considered as it is the dominant recombination route. The recombination resistance depends on the photovoltage V_{PE} as

$$r_{rec} = -\frac{dV_{PE}}{di_{PE}}, \tag{35}$$

where r_{rec} is the measured resistance R_{rec} (in units [Ωm^2]) multiplied by the thickness of the photoelectrode d_{PE}, $r_{rec} = R_{rec} d_{PE}$. i_{PE} is the total current per unit volume in the photoelectrode,

$$i_{PE} = i_g - i_{rec}. \tag{36}$$

Neglecting the current dependence of the electrolyte concentrations, the recombination resistance becomes (eqs. (32, 35 and 36)

$$r_{rec} = \frac{k_B T}{\beta q i_{rec,0}} \sqrt{\frac{c_{I^-}}{c_{I_3^-}}} e^{\frac{-q\beta V_{PE}}{k_B T}}. \tag{37}$$

At small currents, close to open circuit conditions, the concentrations of ion species can be approximated to have their equilibrium values, $c_i \approx c_{i,0}$. The coefficient $i_{rec,0}$ can therefore be determined using eq. (37),

$$i_{rec,0} = \frac{k_B T}{\beta q r_{rec,OC}} \sqrt{\frac{c_{I^-,0}}{c_{I_3^-,0}}} e^{\frac{-q\beta V_{OC}}{k_B T}}, \tag{38}$$

where $r_{rec,OC}$ is the recombination resistance at open circuit and V_{OC} the open circuit voltage. The values for $i_{rec,0}$ and β can be calculated from eq. 38 by measuring $r_{rec,OC}$ at least at two different light intensities as explained in section 5.

It is worth noting that contrary to many other numerical models, except e.g. that of Ferber et al. [4], the present model includes also the influence of iodide and triiodide concentrations on the electron recombination, as evident from eq. (37). Note that the concentration dependence in eq. (37) is a first order approximation, since the concentrations were not differentiated with respect to the cell current when deriving eq. (37). In the numerical simulations, we use directly eq. (32) (as a part of eq. (43)), which is not subject to this approximation.

2.8 Conductivity of the photoelectrode

Assuming that the mobility μ of the conduction band electrons is constant, the conductivity σ of the TiO_2 photoelectrode film can be written as [36]

$$\sigma = q\mu n_e = r_t^{-1} = \sigma_0 e^{\frac{qV_{PE}}{k_B T}}. \tag{39}$$

where r_t [Ωm] is the electron transport resistivity and σ_0 is the conductivity at equilibrium in the dark. The voltage dependence of the conductivity follows from the assumption of "ideal" Boltzmann statistics of the conduction band electrons (eq. 24). Ideal voltage dependence of r_t, and thus σ, has been found also experimentally by impedance spectroscopy [37, 36, 38], although not for all cases [36]. In the absence of a well established physical model for non-ideal electron transport, we use eq. (39) in the present work.

2.9 Substrates

The substrates affect the performance of the cell with their sheet resistance and the photoelectrode substrate also by current leakage to the electrolyte. In high efficiency cells, the current leakage via the substrate is often prevented by using a recombination blocking layer.

The sheet resistance of the substrates R_s can be taken into account with a simple IR-correction to the calculated IV-data, and EIS measurements can be used to determine its value. Note that the sheet resistance and current collector grid are perpendicular to the cross section of the cell. Hence if the model is expanded to 3D the sheet resistance and different current collector structures can be easily added as separate modeling domain. The model for the current collection is shown in our previous work [39].

The current leakage via substrate dominates at the low voltages [9, 11, 36]. It should, however, be noticed that it has only a negligible effect on the IV curve of dye solar cells at high light intensities such as at 1 Sun [7, 10, 11]. Hence, at high light intensities, recombination via substrate has been and can be in many cases omitted. At low light intensities the effect of substrate needs to be taken into account if recombination blocking layer is not employed.

If necessary, the current leakage via the photoelectrode substrate can be modeled. In practice the photoelectrode substrate acts similarly to a counter electrode with a very small i_0 (14). Hence, it can be modeled with the same equations as the counter electrode. The value for i_0 can be measured from a SU-CE cells [11, 40] in open circuit conditions, or, alternatively from a complete DSC with the cell voltage of 0 V with eq. (18). In the latter case, it is assumed that $R_{rec} >> R_{SU}$ at V_{PE}=0. Normally this is a very good assumption e.g. with FTO glass substrates the difference is more than two orders of magnitude at V_{PE}=0 [11].

3 Solving the model with COMSOL Multiphysics

3.1 Application modes and the analysis type

COMSOL Multiphysics is a modeling software that uses the finite element method to solve partial differential equations numerically. The model was built using two ready-made application modes, 'Nernst-Planck' and 'Conductive media DC' [41]. The transient type analysis is embedded in the 'Nernst-Planck' mode. The concentrations of ions and the potential of the electrolyte were solved in the 'Nernst-Planck' mode and the electrode potentials were solved in the 'Conductive Media DC' mode. The porosity of the electrodes is realized by overlapping the electrode domains with the electrolyte domain. The model could also be made in the general mode called 'PDE, General form'. The usage of ready made applications modes is, however, easier. An example of the modeled geometries is shown in Figure 1.

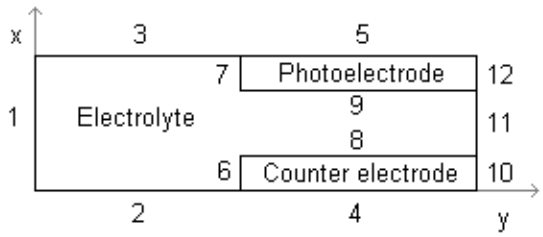

Figure 1: An example of the modeled geometries. The electrode and electrolyte domains are overlapping. The boundaries are marked with numbers from 1 to 12. The dimensions are not in scale.

3.2 Subdomain equations

In the 'Nernst-Planck' mode the current continuity equation from which the potential of the electrolyte is solved has the form

$$\nabla \cdot \left[F \sum_i z_i (-z_i u_{m,i} F c_i \nabla \phi_{el} - D_i \nabla c_i) \right] = F \sum_i z_i R_i, \tag{40}$$

where ϕ_{el} is the potential of the electrolyte and R_i the reaction rate of species i. R_i is $\nabla \cdot \mathbf{N}_i$ defined by eq. (4) which relates i_{CE} and i_{PE} to the charge transfer in the electrolyte. The material balance equation for the concentrations has the form (*cf.* eq. (2)

$$\delta_{ts} \frac{\partial c}{\partial t} + \nabla \cdot (-D \nabla c - z u_m F c \nabla \phi_{el}) = R - \mathbf{u} \cdot \nabla c, \tag{41}$$

where δ_{ts} is a time-scaling coefficient, c the concentration being solved, R the reaction rate and $\mathbf{u}$ the velocity as a vector quantity. Because convection in the electrolyte was not taken into account, both x-velocity u and y-velocity v were set to zero. For δ_{ts}, the default value 1 was used. In the 'Nernst-Planck' mode, the concentrations of two of the ion species are solved from eq. (41) and the third one, here c_{Li^+}, directly from electroneutrality condition, eq. (5). In the electrolyte areas that overlap the electrodes, the porosity of the electrode (typically about 50 %) has been taken into account by diving the diffusion coefficients D_i with factor 2.

In the 'Conductive Media DC' mode, the current continuity equation is of the form

$$-\nabla \cdot d(\sigma \nabla V - \mathbf{J}^e) = dQ_j, \tag{42}$$

where d denotes thickness, $\mathbf{J}^e$ the external current density, and Q_j the current source. For d, the default value 1 was used and both components of $\mathbf{J}^e$ were set to zero. All conductivities were modeled as isotropic. Q_j refers to current via electrodes i which is entered as a subdomain expression and defined separately in each domain based on eqs. (14), (22), (32) and (25):

$$\text{PE:} \qquad i_{PE} = qa\Phi\eta_{inj}e^{-ax} - i_{rec,0}\left[\sqrt{\frac{c_{I_3^-}}{c_{I^-}}}e^{f\beta V_{PE}} - \sqrt{\frac{c_{I_3^-,0}}{{c_{I^-,0}}^3}}c_{I^-}\right], \tag{43}$$

$$\text{CE:} \qquad i_{CE} = i_0\left[\frac{c_{I^-}}{c_{I^-,0}}e^{-\alpha f\eta_{CE}} - \sqrt{\frac{c_{I_3^-}c_{I^-,0}}{c_{I^-}c_{I_3^-}}}e^{(1-\alpha)f\eta_{CE}}\right]. \tag{44}$$

3.3 Boundary conditions

The boundary conditions used in modeling are gathered in Tables 1 and 2. The equations in Table 1 correspond to the geometry of Figure 1, where the counter electrode is modeled as a domain. In the case where the counter electrode is modeled as a boundary, boundaries 6, 8, and 10 vanish and the insulating conditions at boundary 4 are replaced with the flux and inward current flow conditions written in Table 2. The current leakage via substrate could be taken into account with similar equations as shown for boundary type counter electrode (Table 2) at boundary 5.

The 'Conductive media mode' calculates the potential ϕ in the different domains. The voltage over the cell V_{cell} is controlled by setting constant potentials at the counter electrode and photoelectrode boundaries that indicate contacts to the external circuit. In the model, zero potential level is selected to be at the counter electrode boundary. Therefore, the value of the potential at the photoelectrode corresponds to the value of V_{cell} (Table 1). This way, the direction and magnitude of the current through the cell is determined by the voltage.

Table 1: Boundary conditions in the geometry of Figure 1. The zero potential was selected to be at the counter electrode (boundary 4), hence the potential at the photoelectrode substrate (boundary 5) is then equal to the cell voltage.

Variable	Boundary	Condition	Equation
c_i	1, 2, 3, 4, 5, 10, 11, 12	Insulation/Symmetry	$\mathbf{n} \cdot \mathbf{N}_i = 0$
ϕ_{el}	1, 2, 3, 4, 5, 10, 11, 12	Electric insulation	$\mathbf{n} \cdot \mathbf{J} = 0$
ϕ_{PE}	7, 9, 12	Electric insulation	$\mathbf{n} \cdot \mathbf{J} = 0$
	5	Electric potential	$\phi_{PE} = V_{cell}$,
ϕ_{CE}	6, 8, 10	Electric insulation	$\mathbf{n} \cdot \mathbf{J} = 0$
	4	Electric potential	$\phi_{CE} = 0$

Table 2: Boundary conditions at boundary 4 in Figure 1 in the case of a boundary counter electrode.

Variable	Condition	Equation
c_i	Flux	$-\mathbf{n} \cdot \mathbf{N}_i = \frac{s_i}{nF} i$
ϕ_{el}	Inward current flow	$-\mathbf{n} \cdot \mathbf{J} = i$

4 Experimental Methods

The parameters i_0, $i_{rec,0}$, β, σ_0 and $D_{I_3^-}$ in the model were determined experimentally by studying the I-V characteristics and impedance spectra of dye solar cells and counter electrode cells built on glass substrates. The DSCs were assembled using materials and methods described in [40] with the exception that there was a 4 nm compact ALD TiO_2 blocking layer on the photoelectrode FTO-glass substrate to prevent recombination from the substrate [11]. The area of the photoelectrode was 0.4 cm^2. In the CE-CE cells, 40 μm thick Surlyn ionomer resin film 1601 was used instead of the 25 μm thick 1702 film used in [40] and in the electrolyte, 0.05 M I_2 was used instead of 0.03 M.

I-V and electrochemical impedance spectroscopy (EIS) measurements were performed using Zahner Elektrik's IM6 Impedance Measurement unit (Zahner Elektrik) and Autolab PGSTAT302N (Eco Chemie). The I-V and EIS measurements of the complete DSCs were performed at different light intensities in OC. The measurements were made in a black box and a LED of 639 nm wavelength was applied as a light source. The I-V measurements of the CE-CE cells were taken in the dark in the voltage range -1 V–1 V and with a scan rate of 20 mV/s. All the EIS measurements were made in the frequency range 100 kHz–100 mHz and with a 10 mV amplitude. The equivalent circuit analysis was similar to our previous publications [11, 40], using the ZView2 software.

5 Material parameters

The constants and experimental parameters used for modeling are in Table 4. The initial concentrations of ion species are those of the electrolyte composition used in the measured DSCs. The absorption coefficient a of the dyed photoelectrode has been obtained through optical measurements at the 640 nm wavelength. This wavelength matches sufficiently well the 639 nm LED used in measuring the DSCs. σ_0 was determined according to eq. (39) using R_t data from the EIS measurements (Table 3, voltage point 0.4635 V).

The diffusion coefficient of I_3^- was measured from a CE-CE cell with electrolyte layer thickness of 40 μm and I_3^- concentration of 50 mol/m^3. I-V measurements (Figure 2) were made to determine the limiting current density i_{lim}, here the value was 23.42 mA/cm^2. Using eq. (6), the resulting value for $D_{I_3^-}$ was $4.8545 \cdot 10^{-10}$ m^2/s. The diffusion coefficients are assumed to be equal for all ion species. This is a common practice in these types of models since it is difficult to determine the separate coefficients reliably.

The recombination resistance of the PE and the charge-transfer resistance of the CE were determined from the impedance spectra at three different OC voltages

corresponding to different light intensities shown in Table 3. The coefficient i_0 was then calculated from eq. (18) for all values of R_{CT} and the average is shown in Table 4. With two values for R_{rec}, $i_{rec,0}$ and β can be solved from a pair of equations using

Table 3: Resistance values at different light intensities i.e. different OC voltages defined via impedance spectroscopy.

V_{OC} (V)	R_{CT} (Ω)	R_{rec} (Ω)	R_T (Ω)	R_s (Ω)
0.4635	-	3407.8	1758.9	14.805
0.5985	33.650	215.24	-	15.931
0.6260	30.683	112.57	-	14.294
0.6430	28.479	74.050	-	13.411

eq. (38). $i_{rec,0}$ and β (Table 4) were averaged from the three values obtained by making all the possible combinations of the different values for R_{rec}, from the above mentioned three different light intensities.

Table 4: Constants and parameters used in the model.

Constants	Symbol	Value
Boltzmann constant	k_B	$1.380665 \cdot 10^{-23}$ J/K
Elementary charge	q	$1.60218 \cdot 10^{-19}$ C
Faraday constant	F	96485.3 C/mol
Gas constant	R_{gas}	8.31447 J/(molK)
Number of transferred electrons	n	2
Stoichiometric coefficient of I^-	s_{I^-}	-3
Stoichiometric coefficient of I_3^-	$s_{I_3^-}$	1
Stoichiometric coefficient of Li^+	s_{Li^+}	0
Parameters		
Absorption coefficient	a	0.04 $1/\mu m$
Charge transfer current density	i_0	26.073 A/m^2
Conductivity of TiO_2 at equilibrium	σ_0	$3.099 \cdot 10^{-12}$ S/m
Diffusion coefficients of all ion species	D_{I^-}, $D_{I_3^-}$, D_{Li^+}	$4.8545 \cdot 10^{-10}$ m^2/s
Ideality factor	β	0.618
Initial concentration of I^-	$c_{I^-,0}$	470 mol/m^3
Initial concentration of I_3^-	$c_{I_3^-,0}$	30 mol/m^3
Initial concentration of Li^+	c_{Li^+}	500 mol/m^3
Equilibrium recombination current density	$i_{rec,0}$	$13.731 \cdot 10^{-10}$ A/cm^2
Temperature	T	298.15 K
Transfer coefficient	α	0.5
Thickness of the TiO_2 layer	d_{PE}	15 μm
Distance between the electrode substrates	d	20 μm

6 Verification against experimental data

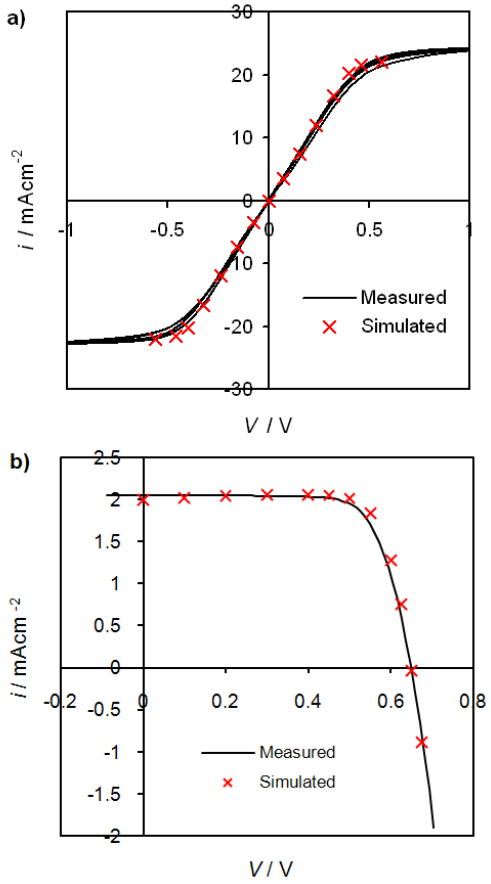

Figure 2: Measured and simulated I-V characteristics of a) a CE-CE cell and b) a complete DSC. The resistance parameters are given in Table 3.

The model was verified against experimental data by comparing measured I-V curves of a DSC as well as CE-CE with the corresponding simulated I-V curves. For this purpose, the inactive boundaries, i.e. boundaries 2 and 3 in Figure 1 were omitted, which rendered the simulation essentially one-dimensional. This correspondence to the real situation in the measured CE-CE cells, where the Pt catalyst layer covers the whole substrate surface. It is also a valid approximation of the situation in a complete DSC, as shown later in section 7.3.

The catalyst layer in the measured DSC and CE-CE cell was a very thin Pt layer which was modeled as a boundary counter electrode. The photoelectrode in the DSC was equipped with a recombination blocking layer meaning that current leakage via substrate can be omitted. The light source in the measurement was a red LED which gave approximately 0.15 Sun illumination. This way heating of the DSC could be prevented as it is difficult to cool thick glass based DSCs at full 1 sun illumination.

The correspondence of the simulated and measured I-V data of the CE-CE cell is good (Fig. 2). There are small deviations around the voltages ± 0.3 V, where the gradient of the curve begins to decrease. These are, however, smaller than the deviations between the different measured curves, which are due to hysteresis and differences between I-V sweeps. Hence, the measured and the simulated data are in practice the same when taking into account the measurement accuracy.

The measured and simulated data of the complete dye solar cells (Fig. 2 b) are also corresponding. This is in fact a very good result when taking into account that the only model parameter which was fixed according to the experimental I-V curve was the product $\Phi\eta_{inj}$ so that the i_{SC} of the measured and simulated data matched. In other words, with the photocurrent generation adjusted, the model predicts well the experimentally observed V_{OC} and fill factor, as well as the slope of the I-V curve, using independently determined parameters.

7 Results and discussion

As already pointed out, the main new feature of the present numerical DSC model arises from the capability to run transient 2D simulations of the cell operation at the scale of the complete devises. However, whether such simulations of the cell are actually needed in practice is not obvious. Being a thin layer electrochemical cell where several millimetres wide electrode are situated at a distance of only few tens of micrometers from each other, it is usually a fair assumption that the electric current flows through the device exactly perpendicular to the co-planar electrodes, which makes 1D simulations valid for most practical cases. The need for 2D simulations arises only when the one-dimensionality is broken by some structural features in the lateral dimensions of the cell. In the rest of the paper, we demonstrate this by investigating one such case, which in fact, is a standard type laboratory scale DSC. The transient analysis on the other hand gives useful information related to e.g. the expected time to reach stead state.

In the simulations, we will be looking at the cross-section of a DSC that has a 15 μm thick and 4 mm wide PE film (dyed nanoporous TiO_2, in Fig. 1) facing a 5 mm wide planar CE (thin film of Pt, regions 2 and 4 in Fig. 1), both sitting on parallel FTO coated glass substrates that are separated from each other with 20 μm thick edge sealant, so that there is 5 μm of free electrolyte between the PE and CE. While at the CE, the catalyst layer covers the entire FTO surface wetted by the electrolyte, at the PE side of the cell there is 0.5 mm passive area that is not covered by the PE film, at the both sides of the PE film. This is the typical structure of a small sized DSC laboratory test cell used for material testing and experimental studies [14, 42]. Since the PE and CE are centered with respect to each other, the simulations need to be done only for the half of the cross section of the cell. I.e. the vertical borders 10, 11 and 12 on the right of Fig. 1 can be considered as a symmetry axis cutting

the cell half at the center the cell. The cell is assumed to have infinite length in the dimension perpendicular to the paper, which corresponds roughly to a long unit cell in a large DSC module.

In this typical DSC geometry, the exact one-dimensionality is broken by the different size of the PE and CE, which creates an edge region next to the PE containing an excess volume of electrolyte as well as extra catalytic CE surface area. In the following simulations we take a look what happens in this edge region under normal cell operation, and how it affects the cell performance. This issue seems to have been completely neglected in the previous literature. More specifically, we investigate the following phenomena, taking place in the typical DSC:

1. With time-dependent simulation of the 2D distribution of tri-iodide concentration in the cell, we investigate how the excess electrolyte volume in the edge region influences mass transport in the rest of the cell as well as the time to reach steady state operation after turning on illumination. This has implications to the cell performance and its experimental evaluation. In this scenario, it is assumed that any influence of charge trapping and detrapping is fast relative to the transient electrolyte effects of interest.

2. By simulation of the current density distribution at the counter electrode, we investigate to which extent the extra catalyst material in the edge region is actually utilized in the charge transfer reactions. Any un-utilized catalyst increases the solar cell manufacturing costs without contributing to its output power.

Unless otherwise mentioned, the same cell geometry (described above) applies to both of the cases. The material parameters are the same as for the simulated I-V curve in Figure 2b.

7.1 2D distribution of tri-iodide and time to reach the steady state

The simulation starts from a situation where the concentration of ions is even across the cell, which corresponds to the real life situation of the cell being in the dark and unpolarized. At t=0, light intensity corresponding to ca. 0.15 suns is turned on and the solar cell is polarized close to the short circuit conditions (V_{cell} = 0.2 V).

Fig. 3 shows the evolution of the tri-iodide concentration in the cell. Note how the I_3^- becomes almost completely depleted from the edge region next the PE (on the left) and accumulates in front of the PE. This is a rather unexpected result that will be discussed below.

The time required to reach the final steady state distribution can be examined by selecting a point in the modeled domain and plotting its values against time. In this

case, the lower right corner in Fig. 3, i.e. center of the cell on the CE, stabilized last. Fig. 4 shows that this took about 1000 s. Note how right at the start of the simulation, there is a fast drop in the I_3^- concentration at the CE from its initial value of 30 mol m$^-$1 in 1 s to ca. 26.5 mol m$^-$1. This transient is very fast and it is partially established already at the initialization of the numerical simulation (Fig. 3 $t = 0$ s). Note that at time $t = 0$, the simulation gives actually the first calculated solution which already deviates from the initial settings. This transient corresponds to the diffusion of tri-iodide across the distance $d = 20$ μm between the PE and CE as the current in the cell starts flowing and the tri-iodide is consumed at the CE. The time required for this can be estimated as $t = \frac{d^2}{D_{I3-}} = 0.8$ s, which is consistent with the time step of 1 s used in the simulation. After the initial transient, a slow recovery of the I_3^- concentration occurs as excess I_3^- available in the edge region diffuses to the area in front of the PE, with the striking result that, at the steady state, the I_3^- concentration at the CE (32 mol m$^-$1) exceeds its initial equilibrium concentration (30 mol m$^-$1) (Fig. 3). In effect, the excess I_3^- of the edge region has moved into to active area of the cell and has been engaged in the cell operation. The time required to reach the steady state corresponds thus to the time it takes for the I_3^- to diffusion across ca. 2 mm in the lateral dimension of the cell, i.e. $t =$ 8200 s, which is roughly the same order of magnitude as the simulation result that gave stabilization time of 1000 s (Fig. 4).

These above observations have the following important practical implications, which we briefly point out here, while leaving their quantitative analysis as a topic of future investigations. Firstly, the increase of the I_3^- concentration in the active area of the cell due to transfer of the excess I_3^- from the edge region improves mass transport between the electrode, so that the mass transport resistance at the counter electrode decreases and the limited current density increases (cf. [14] for the effect of these on cell performance). However, at the same time the I_3^- concentration at the PE will be higher than what it would be without the edge region, which promotes electron recombination and causes additional optical losses due to absorption of light by the I_3^- in the pores of the TiO_2 film. In the same simulation, there was transfer of I^- laterally in the cell, in the opposite direction to I_3^-, i.e. from the PE area to the edge region (not shown). In principle, the decreased I^- concentration can retard regeneration of the dye at the PE. In other words, this cell geometry favors CE performance at the expense of PE performance. We could argue that this is obvious since the CE is larger than the PE, meaning that the current density and thus voltage losses will be lower at the CE than at the PE. However, as shown in the next section, the current density at the CE is confined rather well to the region right opposite to the PE, which implies that the I_3^- distribution is not a result of the current density per se. Instead, as explained in the next Section, it is result of spontaneous adjustment of the current distribution to minimize the overall voltage loss at the CE side of the cell.

The loss of I_3^- from the edge region should correspond to bleaching of the color of the electrolyte in the edge region. We have indeed observed this experimentally by

visual inspection of the solar cells when passing current though them: the brownish-yellow color characteristic to the I_3^- fades in the edge region when the cell is put in operation. The effect could be seen even in blank cells, consisting of two CEs of different size, i.e. the PE replaced with a Pt on FTO, electrically isolated from rest of the substrate by cutting the FTO between the borders 3 and 5 in Fig. 1. This confirms that the effect is due to current passing in the cell, rather than just the illumination of the solar cell.

What we have essentially witnessed here both by simulations and experiments is a color change in the DSC as a function of its operation. This may be an important issue from the point of view of practical DSC product design. Much of the present advantages of DSCs over other photovoltaic technologies are based on its unique visual aspects such as color and semi-transparency, which one might want to fix by the design, rather than allow them to vary depending on the operating conditions.

Change of the electrolyte color upon cell operation can be important also from the point of view of accurate performance characterization of DSC. In fact, the present results may explain why it has been so difficult to obtain a good fit of the IPCE model of DSC to measured IPCE spectra at wavelengths below 500 nm where the light absorption by the I_3^- is strong [43, 44, 33]. Note that IPCE measurements are taken at the short circuit condition, i.e. when current density in the cell is at the maximum. According to the present results even relatively low current density can change the tri-iodide concentration in the active area of the cell, compared to the equilibrium concentration in separate optical sample cells used for determining the electrolyte transmittance experimentally. As a result of the I_3^- accumulation to the active area, the electrolyte transmittance becomes overestimated compared to the real situation in the solar cell.

Also the relatively long time to reach a steady state operation, more than 8 minutes predicted by the simulation, can be problematic, especially in cases where the cell performance is limited by mass transport in the cell. In practice, the slow lateral distribution of the electrolyte species in a polarized cell could cause drift in the cell properties during long measurements. In fact, this could be an explanation to the drift observed often the EIS data of complete DSCs at the low frequencies where the EIS spectrum is dominated by the electrolyte diffusion impedance. The present results gives thus a practical recommendation for building a DSC test cell. In order to avoid electrolyte drift during the measurements, it is advisable cut the thermoplastic (e.g. Surlyn) sealant exactly to the size of the PE film, in order to minimize the edge region in the cell. Note that merely sizing the CE exactly to the size of the PE (e.g. by laser scribing the FTO), would not be sufficient due to the practical difficulty in placing such electrodes exactly opposite each other. This becomes clear from the results in the Section 7.2 below.

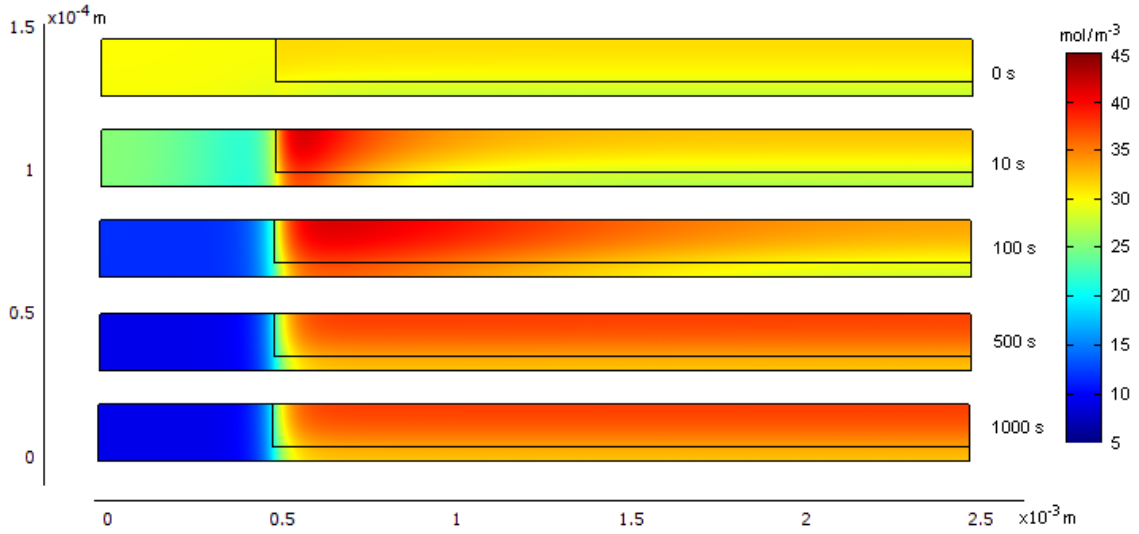

Figure 3: The concentration profile [mol/m^3] of I_3^- with a cell voltage 0.2 V at different points in time (0 s, 10 s, 100 s, 500s, 1000 s). The electrodes in the studied cell had different width as indicated with the borders of the geometry (see Fig. 1): the counter electrode was full width (2.5 mm) and the photoelectrode only 2 mm, leaving 0.5 mm of inactive substrate at the PE side (on the left in the figure). Note that the scaling of the x- and y-axis are different.

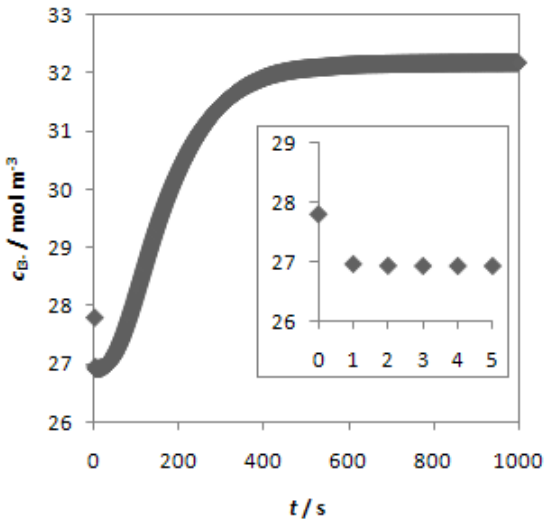

Figure 4: The concentration of I_3^- as a function of time t in the low right corner of the modelled domain (Fig. 3). The initial concentration was 30 mol m$^-$3. The inset shows the up-scale of the first 5 s.

7.2 Current distribution at the counter electrode

In the preparation of a typical laboratory scale DSC, the Pt catalyst is deposited on the FTO coated glass substrate by drop casting a Pt precursor solution on it.

In the solar cell, the Pt catalyst covers thus the whole electrolyte wetted FTO surface bordered by the edge sealant, and as a result the CE is larger than the PE [42]. Whether this extra Pt at the edge region of the cell contributes to the overall CE performance in the operating cell is a relevant question regarding accurate device characterization, but it is important also for the optimization of the cost-performance ratio of DSCs.

Figure 5 shows the current distribution at the counter electrode in the same simulation as discussed above. It can be clearly seen that the current density, that is restricted to flow through the dye-sensitized TiO_2 film at the PE side, distributes itself laterally at the CE side only about 50 μm beyond the edge of the PE film (Fig. 5 b). Hence, it can be concluded that the Pt deposited in the edge region of the cell is almost completely unutilized in the cell operation.

The reason for the confinement of the current right opposite of PE is the very short distance between the electrodes (5 μm) compared to the lateral dimensions of the cell, or more precisely, the high voltage losses associated with transfer of current over long distances laterally in the electrolyte. Note that the current density distribution adjusts itself to minimize the overall voltage loss in the cell, i.e. the current always finds the path of least resistance. Here, lateral distribution of the current density into the edge region at the CE is effectively restricted by increase of the I_3^- mass transport overvoltage at the CE as a function of distance across which the I_3^- needs to diffuse. Indeed, it was shown in the previous Section that I_3^- is essentially depleted in the edge region even at a moderate cell current density. This corresponds to a mass transport limited condition at the CE surface, making it essentially inactive in the charge transfer process. A further contribution to the current confinement comes from the Ohmic resistance in the electrolyte.

To complete the mental picture of the processes behind the present phenomena, we point out how the dramatic depletion of I_3^- from the edge region in the operating cell (Figure 3) results from the principle of spontaneous current distribution that minimizes the overall voltage loss at the CE side of the cell. This voltage loss is minimized when the current distribution is as uniform as possible, since this minimizes the local current density at the CE surface. The maximum for the uniformity is determined by the ability of the current to flow to the edge region. This ability is limited by the rapid rise in the I_3^- mass transport overvoltage at the CE for a given current density, when the current path length is increased, as already mentioned. As a result, a spontaneous adjustment of the current distribution at the CE takes place, in which as much current density is passed to the edge region as possible without increasing the overall voltage loss, but on the contrary decreasing it. In practice, this corresponds to a local current density at the CE that is right before the onset of the rapid increase in the I_3^- mass transport overvoltage (cf. Figure 14c in ref. [14], the value of which is the lower the longer the distance to the edge of the PE. This value of the current density corresponds to low I_3^- concentration at the CE surface, which explains the depletion of I_3^- in the edge region.

The restricted current distribution at the CE has two practical implications. Firstly, in the performance characterization of DSCs, such as with electrochemical impedance spectroscopy (EIS), the current density and charge transfer resistance (in Ωcm^2) should be calculated based on the area defined by the geometric overlap of PE and CE, which in practice is normally equal to the area of the PE film. This has been a standard practice in our case, as justified by qualitative reasoning based on the internal resistances as discussed above. The present simulation result verifies it quantitatively.

Secondly, from the point of view of industrial manufacturing of DSCs, the result implies that distributing the catalyst to larger areas than that defined by the PE film is waste of catalyst material. Omitting the potentially expensive catalyst at the edge regions of the cell is thus one way to reduce the manufacturing costs without effects on the cell performance. Of course, the best solution would be to omit the edge region altogether, so that the active area losses of the DSC module would be minimized. However, to which extent this can be realized in practice depends on the manufacturing tolerances of a given DSC module technology.

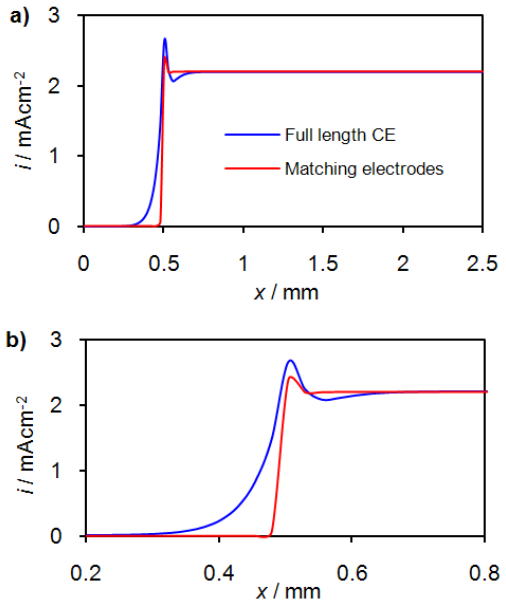

Figure 5: The current profile at the counter electrode in the cases where the counter electrode is max lenght (here 0-2.5 mm) or matching with photoelectrode (here 0.5-2.5 mm). a) The whole simulated profile and b) the profile from 0.2 mm to 0.8 mm.

7.3 Further development and applications

In addition to the edge effects caused by having a larger counter electrode, the model is applicable for many other situations where there is some asymmetry in the

structure or operation of the cell. One important case is the segmented cell method [2, 45, 46, 47], which is a new in-situ technique for aging studies. A typical question related to segmented cells is how quickly the neighbouring segments affect each other, and for this purpose both 2D and transient modeling features are required.

The transient feature can also be applied for analysis of voltage and current steps. Additionally it can be applied to study degradation for instance by introducing leakages in the form of ion fluxes or sink terms at the boundaries.

It would also be interesting to make a real sized 3D model of a DSC. From the theoretical point of view this is easy, but the number of elements to be calculated becomes enormous. The size of the elements is defined in relation to the smallest dimension. In the case of DSCs, the limiting dimension is the thickness of the cell. Scaling the model suitably, the dimensions can be adjusted to the same order of magnitude and the number of studied elements can be reduced to a reasonable level. In a 3D model it would be possible to take into account also the effects of sheet resistance of the substrates and current collector grid.

In addition we want to point out how they could in principle be taken into account to further develop the model. The present model neglects the effect of spatially varying and current dependent iodide concentration on the regeneration of the dye (eq. 4 in [14]). In an operating cell under illumination, the iodide concentration at the photoelectrode is lower than at the equilibrium, as it is constantly consumed in the dye regeneration while its supply from the counter electrode is limited by diffusion [5]. The reduced iodide concentration can in principle decrease the dye regeneration rate and thereby increase direct recombination of electrons with the oxidized dye, apparently diminishing electron injection efficiency. Although there is some indirect experimental evidence of injection limitations due to iodide depletion [5], the significance and theoretical treatment of this effect remains to be clarified.

8 Conclusions

A numerical 2D transient model of dye solar cells was developed using the COMSOL Multiphysics software. The model includes all the important inner components of a dye solar cell: the photoelectrode, the electrolyte, and the counter electrode. The simulated I-V data was verified against the experimental data of a dye solar cell and a symmetric counter electrode - counter electrode cell. The unique features of the model are the capability to simulate spatial distribution and transient phenomena. Here the model was applied to the study of edge effects and revealed that a typical small blank space (0.5 mm) on the photoelectrode side can significantly change the distribution of ions and the time to reach steady state.

In a dye solar cell, where the photoelectrode is smaller than the counter electrode, tri-iodide ions move from the inactive edge region to the active region between the electrodes when photocurrent is flowing. In a normal homogeneous case, the tri-iodide concentration at the counter electrode decreases when current is drawn from the cell. However, in this case with smaller photoelectrode, the excess ions from the edge region actually over compensated the tri-iodide concentration at the counter electrode so that it was higher than the initial equilibrium value. Although having a larger counter electrode significantly affected the ion concentration, it was further shown that the current was driven at the counter electrode through only about 50 μm larger area compared to the photoelectrode. Furthermore, the examination of the stabilization time showed that as much as an 8 minutes' stabilization time was required even when having only this 0.5 mm misalignment between the electrodes. The modelled misalignment between the electrodes is quite typical and its effect on the ion concentration and relatively long stabilization time might explain some common issues such as the drifts in EIS measurements and problems in the fitting of IPCE spectra.

In addition to these examples, the model can be used in the prediction electrochemical performance the dye solar cells and in their design. In particular, the model suits to special cases such as the analysis of segmented cells. The model can easily be developed further to meet the needs of different specific purposes.

9 Acknowledgements

This work was funded by the CNB-e project. We thank Suvi Karvonen and Sonja Auvinen for their suggestions on the implementation of the model in Comsol.

References

[1] Green, M.; Emery, K.; Hishikawa, Y.; Warta, W., *Prog. Photovolt: Res. Appl.*, **2009**, 17, 85-94.

[2] Miettunen, K.; Halme, J.; Lund, P., *Electrochem. Comm.*, **2009**, 11, 25-27.

[3] Papageorgiou, N.; Grätzel, M.; Infelta, P., *Sol. Energy Mater. Sol. Cells*, **1996**, 44, 405-438.

[4] Ferber, J.; Stangl, R.; Luther, J., *Sol. Energy Mater. Sol. Cells*, **1998**, 53, 29-54.

[5] Papageorgiou, N.; Liska, P.; Kay, A.; Grätzel, M., *J. Electrochem. Soc*, **1999**, 146, 898-907.

[6] Hyk, W.; Augustynski, J., *J. Electrochem. Soc.*, **2006**, 153, A2326-A2341.

[7] Ferber, J.; Luther, J., *J. Phys Chem. B*, **2001**, 105, 4895-4903.

[8] Bard, A.; Faulkner, L., *Electrochemical Methods*, John Wiley & Sons, Inc, **2001**.

[9] Cameron, P.J.; Peter, L.M.; Hore, S., *J. Phys. Chem. B*, **2005**, 109, 930-936.

[10] Hore, S.; Kern, R., *Appl. Phys. Lett.*, **2005**, 87, 263504.

[11] Miettunen, K.; Halme, J.; Vahermaa, P.; Saukkonen, T.; Toivola, M.; Lund, P., *J. Electrochem. Soc.*, **2009**, 156, 876-883.

[12] Gagliardi, A.; Auf der Mauer, M.; Gentilini, D.; Di Carlo, A., *J. Comput. Electron.*, **2009**, 8, 398-409.

[13] Cao, F.; Oskam, G.; Meyer, G.J.; Searson, P.C., *J. Phys. Chem.*, **1996**, 100, 17021-17027.

[14] Halme, J.; Vahermaa, P.; Miettunen, K.; Lund, P., *Adv. Mat.*, **2010**, 22, E210-E234.

[15] Tanaka, S., *Jpn. J. Appl. Phys.*, **2001**, 40, 97-107.

[16] Hottinen, T.; Himanen, O.; Karvonen, S.; Nitta, I., *J. Power Sources*, **2007**, 171 113-121.

[17] Hoshikawa, T.; Yamada, M.; Kikuchi, R.; Eguchi, K., *J. Electrochem. Soc.*, **2005**, 152, E68-E73.

[18] Luque, A.; Hegedus, S.(ed.), *Handbook of Photovoltaic Science and Engineering*, John Wiley & Sons Ltd, England, **2003**, 663-678.

[19] Imoto, K.; Takahashi, K.; Yamaguchi, T.; Komura, T.; Nakamura, J.; Murata, K., *Sol. Energy Mat. Sol. Cells*, **2003**, 79, 459-469.

[20] Murakami, T.; Ito, S.; Wang, Q.; Nazeeruddin, Md.K.; Bessho, T.; Cesar, I.; Liska, P.; Humphry-Baker, R.; Comte, P.; Pechy, P.; Grätzel, M., *J. Electrochem. Soc.*, **2006**, 153, A2255-A2261.

[21] Bisquert, J.; Mora-Seró, I., *J. Phys. Chem. Lett.*, **2010**, 1, 450-456.

[22] Villanueva-Cab, J.; Wang, H.; Oskam, G.; Peter, L.M., *J. Phys. Chem. Lett.*, **2010**, 1, 748-751.

[23] Newman, J.S., *Electrochemical Systems 2nd ed.*, Prentice-Hall, New Jersey, **1991**.

[24] Attwood, D.; Mosquera, V.; Lopez-Fontan, J.L.; Garcia, M.; Sarmiento, F., *J. Colloid Interf. Sci.*, **1996**, 184, 658-662.

[25] Wasserman, E.; Felmy, A.R.; Chilakapati, A., *Colloid. Surface. B*, **2000**, 18, 19-29.

[26] Zabolotsky, V.I.; Nikonenko, V.V.; Pismenskaya, N.D.; Laktionov, E.V.; Urtenov, M.K.; Strathmann, H.; Wessling, M.; Koops, G.H., *Sep. Purif. Technol.*, **1998**, 14, 255-267.

[27] Constantin, D.; Siwy, S., *Phys. Rev. E*, **2007**, 76, 041202.

[28] Wang, X.; Xue, J.; Wang, L.; Gu, W.; Zhang, W.; Wang, Y.; Liu, Q.; Ji, H.; Ouyang, Q., *J. Phys. D Appl. Phys.*, **2007**, 40, 7077-7084.

[29] Hauch, A.; Georg, A., *Electrochim. Acta*, **2001**, 46, 3457-3466.

[30] Vetter, K.J., *Electrochemical kinetics*, Academic Press Inc., **1967**, 475.

[31] Huang, S.Y.; Schlichthörl, G.; Nozik, A.J.; Grätzel, M.; Frank, A.J., *J. Phys. Chem. B*, **1997**, 101, 2576-2582.

[32] Liu, Y.; Hagfeldt, A.; Xiao, X.-R.; Lindquist, S.-E., *Sol. Energy Mat. Sol. Cells*, **1998**, 55, 267-281.

[33] Barnes, P.R.F.; Liu, L.; Li, X.; Anderson, A.Y.; Kisserwan, H.; Ghaddar, T.H.; Durrant, J.R.; O'Regan, B.C., *Nano Lett.*, **2009**, 9, 3532-3538.

[34] Grätzel, M., *Inorg. Chemi.*, **2005**, 44, 6841-6851.

[35] Bisquert, J.; Fabregat-Santiago, F.; Mora-Seró, I.; Garcia-Belmonte, G.; Gimenes, S., *J. Phys. Chem. C*, **2009**, 113, 17278-17290.

[36] Fabregat-Santiago, F.; Bisquert, J.; Garcia-Belmonte, G.; Boschloo, G.; Hagfeldt, A., *Sol. Energy Mat. Sol. Cells*, **2005**, 87, 117-131.

[37] Wang, Q.; Ito, S.; Grätzel, M.; Fabregat-Santiago, F.; Mora-Seró, I.; Bisquert, J.; Bessho, T.; Imai, H., *J. Phys. Chem. B*, **2006**, 110, 25210-25221.

[38] Jennings, J.R.; Li, F.; Wang, Q., *J. Phys. Chem. C*, **2010**, 114, 14665-14674.

[39] Toivola, M.; Peltola, T.; Miettunen, K.; Halme, J.; Lund, P., *J. Nanosci. Nanotechnol.*, **2010**, 10, 1-7.

[40] Miettunen, K.; Halme, J.; Toivola, M.; Lund, P., *J. Phys. Chem. C*, **2008**, 112, 4011-4017.

[41] *Chemical Engineering Module User's Guide*, COMSOL AB, version November 2008.

[42] Ito, S.; Murakami, T.N.; Comte, P.; Liska, P.; Grätzel, C.; Nazeeruddin, M.K.; Grätzel, M., *Thin Solid Films*, **2008**, 516, 4613-4619.

[43] Halme, J.; Boschloo, G.; Hagfeldt, A.; Lund, P., *J. Phys. Chem. C*, **2008**, 112, 5623-5637.

[44] Barnes, P.R.F.; Anderson, A.Y.; Koops, S.E.; Durrant, J.R.; O'Regan, B.C., *J. Phys. Chem. C*, **2009**, 113, 1126-1136.

[45] Miettunen, K.; Halme, J.; Lund, P., *J. Phys. Chem. C*, **2009**, 113, 10297-10302.

[46] Asghar, M.I.; Miettunen, K.; Halme, J.; Vahermaa, P.; Toivola, M.; Aitola, K.; Lund, P., *Energy Environ. Sci.*, **2010**, 3, 418-426.

[47] Zaban, A.; Zhang, J.; Diamant, Y.; Melemed, O.; Bisquert, J., *J. Phys. Chem. B*, **2003**, 107, 6022-6025.